Journal of Power Sources 196 (2011) 8413–8423

Contents lists available at ScienceDirect

Journal of Power Sources

journal homepage: www.elsevier.com/locate/jpowsour

Modeling and control of a portable proton exchange membrane fuel cell–battery power system☆

Yan Zhang, Biao Zhou*

Department of Mechanical Automotive & Material Engineering, University of Windsor, ON N9B3P4, Canada

ARTICLE INFO

Article history:
Received 16 February 2011
Received in revised form 10 May 2011
Accepted 12 May 2011
Available online 6 June 2011

Keywords:
Fuel cell–battery hybrid power system
System modeling
System control
Power management
Portable power system
Experimental study

ABSTRACT

A portable proton exchange membrane (PEM) fuel cell–battery power system that uses hydrogen as fuel has a higher power density than conventional batteries, and it is one of the most promising environmentally friendly small-scale alternative energy sources. A general methodology of modeling, control and building of a proton exchange membrane fuel cell–battery system is introduced in this study. A set of fuel cell–battery power system models have been developed and implemented in the Simulink environment. This model is able to address the dynamic behaviors of a PEM fuel cell stack, a boost DC/DC converter and a lithium-ion battery. To control the power system and thus achieve proper performance, a set of system controllers, including a PEM fuel cell reactant supply controller and a power management controller, were developed based on the system model. A physical 100 W PEM fuel cell–battery power system with an embedded micro controller was built to validate the simulation results and to demonstrate this new environmentally friendly power source. Experimental results demonstrated that the 100 W PEM fuel cell–battery power system operated automatically with the varying load conditions as a stable power supply. The experimental results followed the basic trend of the simulation results.

1. Introduction

Fuel cells, a promising next-generation power source, are widely used in both automotive and stationary applications due to their high power density and low emissions. A proton exchange membrane (PEM) fuel cell is an electrochemical device in which the energy of an electrochemical reaction is converted directly into electricity by combining hydrogen fuel with oxygen from the air with heat as the bypass [1].

A PEM fuel cell that operates in low temperature conditions is suitable for the portable power application. However, PEM fuel cells have issues working independently as a power system. A rapid voltage drop and a slow response to the load demand are the primary critical issues, as most electronic devices require stabilized power and fast transient response. Thus, energy storage devices, such as fast charge and discharge battery and power regulation devices, such as DC/DC converters, are required to work with the PEM fuel cell to form a power system to provide regulated, fast-response power to a variable load.

A typical PEM fuel cell–battery power system consists of a PEM fuel cell stack as the main power source, a buck or boost DC/DC converter as the power conditioning device and a secondary battery power source.

For the best understanding of the PEM fuel cell operation, PEM fuel cell modeling is required to numerically examine the PEM fuel cell system. The basic concept of the fuel cell and the general mathematical model has been introduced in the literature [1–3]. Previously, many improved PEM fuel cell mathematical models have been published [4–12]. Most of these are intended for PEM fuel cell steady-state simulation or for the sizing of PEM fuel cell parameters. Due to the complexity and heavy calculative load of these models, they are not suitable for control design pursuers. To control and operate a PEM fuel cell system at an optimal condition and to maintain high performance of the fuel cell system, a simplified, control-oriented model is required for the control design. Pukrushpan et al. first developed a dynamic model that is suitable for a control study of fuel cell systems [13]. They simplified existing models to make a sufficiently simple model that can simultaneously address the major PEM fuel cell transient and behavior and significantly reduce the complexity and computational load. This simplified model ensured that the controls for the PEM fuel cell could be rapidly developed. Later, several improved control-oriented models were published [14–16]. These models use the same principle to derive the PEM fuel cell model and add either a temperature effect model or a humidifier model to the control-oriented PEM fuel cell model.

After the control-oriented PEM fuel cell model was well developed and widely implemented, the control design for PEM fuel cell

☆ Section 5.4 has been previously presented in ASME 8th International Conference on Fuel Cell Science, Engineering and Technology, 2010.

* Corresponding author. Tel.: +1 519 253 3000x2630; fax: +1 519 973 7007.
E-mail address: bzhou@uwindsor.ca (B. Zhou).

0378-7753/$ – see front matter © 2011 Elsevier B.V. All rights reserved.
doi:10.1016/j.jpowsour.2011.05.022

Nomenclature

a_i	water activity
A_{fc}	fuel cell active area (cm^2)
c_v	water concentration ($mol\,m^{-3}$)
C_p	specific heat capacities ($J\,kg^{-1}\,K^{-1}$)
D_ω	diffusion coefficient ($m^2\,s^{-1}$)
E_0	open circuit voltage (V)
F	Faraday constant (F = 96,485)
i	current density ($A\,cm^{-2}$)
I_0	exchange current density ($A\,cm^{-2}$)
i_{batt}	battery current (A)
i_d	low frequency current dynamics (A)
i_{max}	limiting current (A)
I	current (A)
m	mass (kg)
$\dot{m}$	mass flow rate ($kg\,s^{-1}$)
M	molecular mass ($kg\,mol^{-1}$)
n	number of cells
n_d	electro-osmotic coefficient
p	pressure (Pa)
p_{sat}	vapor saturation pressure (Pa)
Q	maximum battery capacity (Ah)
Q_{ext}	extracted capacity (Ah)
Q_{exp}	exponential capacity ($(Ah)^{-1}$)
R	gas constant (=8.314 $J\,mol^{-1}\,K^{-1}$)
R_c	equivalent series resistor of the capacitor (Ω)
R_L	body resistor of the inductor (Ω)
t_m	thickness of membrane (Ω)
T	temperature (K)
V	over potential (V)
V_{exp}	exponential voltage (V)
W	work (J)
σ_m	membrane conductivity ($\Omega^{-1}\,cm^{-1}$)
γ	ratio of the specific heat capacities of the gas
η_{cp}	isentropic efficiency
λ_{O_2}	oxygen excess ratio
λ_{H_2}	hydrogen excess ratio
λ_m	membrane water content
ϕ	relative humidity
ω_{atm}	air humidity ratio

Subscripts

a	air
act	activation loss
atm	atmosphere
an	anode
ca	cathode
cell	single cell
conc	concentration loss
fc	fuel cell
gen	generated
H_2	hydrogen
in	inlet
membrane	across membrane
N_2	nitrogen
ohm	ohmic loss
out	outlet
O_2	oxygen
reacted	reacted
st	stack
v	water vapor

system was simplified. All of the known control methods can be applied to PEM fuel cell applications. A number of publications have been released [13,15,17,18] with different control strategies (e.g., linear, non-linear, and fuzzy-logic) or for different control purposes in fuel cell operation (e.g., flow control, humidity control, and pressure control).

As the major application of the PEM fuel cell stack, the PEM fuel cell–battery power system is widely used in automotive or stationary applications. The PEM fuel cell–battery power system, including the system design, the modeling and the power management system, has been discussed in the literature [19–24]. However, the fuel cell dynamics flow behaviors were typically neglected and a PEM fuel cell equivalent circuit was used to represent the PEM fuel cell model when the PEM fuel cell stack was modeled. This could reduce the complexity of the model; however, the dynamic flow behavior of the fuel cell is the key component in PEM fuel cell performance. Neglecting the dynamic flow behavior of the fuel cell could result in a significant reduction in the model accuracy. The PEM fuel cell–battery power systems in these publications may have different topologies; however, the power management strategies all have a similar philosophy, which is a balanced power distribution between the fuel cell and the battery to satisfy the load demand.

2. PEM fuel cell stack model

Many PEM fuel cell stack models have been previously proposed. Currently, the best control-oriented PEM fuel cell stack model was developed by Pukrushpan et al. They developed a simplified dynamic model that is suitable for a fuel cell control study [13]. In the model, the temperature of the fuel cell stack was assumed to be constant. This assumption reduced the order of the PEM fuel cell stack model, the simulation time and the complexity. In contrast, the temperature of the fuel cell stack can be controlled using a separate thermal management system. Thus, this assumption is reasonable.

The PEM fuel cell stack model introduced in this study is primarily based on this model. A PEM fuel cell stack model consists of two components: the PEM fuel cell thermodynamics and the electrochemical reaction.

2.1. Dynamic flow model in PEM fuel cell

For the operation of the PEM fuel cell, the thermodynamic model is the major factor that dominates the fuel cell performance and stability.

In this model, the law of mass conservation was used to address the mass flow rate of oxygen, nitrogen, and vapor in the cathode and the hydrogen and vapor in the anode [13].

2.1.1. Mass flow governing equations

Mass conservation law was used to derive the mass flow rate of oxygen, nitrogen, and vapor in the cathode and the hydrogen and vapor in the anode [13].

On the cathode side, this results in the following equations:

$$\frac{dm_{O_2,ca}}{dt} = \dot{m}_{O_2,ca,in} - \dot{m}_{O_2,ca,out} - \dot{m}_{O_2,reacted} \quad (1)$$

$$\frac{dm_{N_2,ca}}{dt} = \dot{m}_{N_2,ca,in} - \dot{m}_{N_2,ca,out} \quad (2)$$

$$\frac{dm_{v,ca}}{dt} = \dot{m}_{v,ca,in} - \dot{m}_{v,ca,gen} + \dot{m}_{v,memberane} \quad (3)$$

On the anode side, this results in the following equations:

$$\frac{dm_{H_2,an}}{dt} = \dot{m}_{H_2,an,in} - \dot{m}_{H_2,ca,out} + \dot{m}_{H_2,reacted} \quad (4)$$

$$\frac{dm_{v,an}}{dt} = \dot{m}_{v,an,in} - \dot{m}_{v,an,out} + \dot{m}_{v,membrane} \quad (5)$$

The electrochemical principle was used to calculate the rates of oxygen consumption, water production, and the hydrogen consumption rate from the stack current, I_{st}:

$$\dot{m}_{O_2,reacted} = M_{O_2} \times \frac{nI_{st}}{4F} \quad (6)$$

$$\dot{m}_{v,ca,gen} = M_v \times \frac{nI_{st}}{2F} \quad (7)$$

$$\dot{m}_{H_2,reacted} = M_{H_2} \times \frac{nI_{st}}{2F} \quad (8)$$

where n is the number of cells in the stack and F is the Faraday number, which is equal to 96,485 C mol^{-1}.

2.1.2. Stack pressure change

In this model, all gases were assumed to obey the ideal gas law and the temperatures inside the cathode and anode were assumed to be equal to the stack temperature [13]. Then the partial pressures of oxygen (p_{O_2}), nitrogen (p_{N_2}), the cathode vapor ($p_{v,ca}$), hydrogen (p_{H_2}), the anode vapor ($p_{v,an}$), and the relative humidity (ϕ) were calculated using the ideal gas law based on the masses of oxygen (m_{O_2}), nitrogen (m_{N_2}), the cathode vapor ($m_{v,ca}$), hydrogen (m_{H_2}), the anode vapor ($m_{v,an}$), and the stack temperature (T_{fc}).

In the cathode, the following equations were used.

Oxygen partial pressure:

$$p_{O_2,ca} = \frac{m_{O_2,ca}R_{O_2}T_{st}}{V_{ca}} \quad (9)$$

Nitrogen partial pressure:

$$P_{N_2,ca} = \frac{m_{N_2,ca}R_{N_2}T_{st}}{V_{ca}} \quad (10)$$

Vapor partial pressure:

$$p_{v,ca} = \frac{m_{v,ca}R_vT_{st}}{V_{ca}} \quad (11)$$

Partial pressure of dry air in cathode:

$$p_{a,ca} = p_{O_2,ca} + p_{N_2,ca} \quad (12)$$

Total cathode pressure:

$$p_{ca} = p_{a,ca} + p_{v,ca} \quad (13)$$

In the anode, the following equations were used.

Hydrogen partial pressure:

$$p_{H_2,an} = \frac{m_{H_2,an}R_{H_2}T_{st}}{v_{an}} \quad (14)$$

Vapor partial pressure:

$$p_{v,an} = \frac{m_{v,an}R_vT_{st}}{V_{an}} \quad (15)$$

Total anode pressure:

$$p_{an} = p_{H_2,an} + p_{v,an} \quad (16)$$

2.1.3. Relative humidity (RH) inside stack

Relative humidity in cathode:

$$\phi_{ca} = \frac{p_{v,ca}}{p_{sat}(T_{st})} \quad (17)$$

Relative humidity in anode:

$$\phi_{an} = \frac{p_{v,an}}{p_{sat}(T_{st})} \quad (18)$$

where p_{sat} is the vapor saturation pressure that varied with temperature. In this model, T_{st} was a constant value; therefore the vapor saturation pressure was also a constant.

2.1.4. Water transfer across the membrane

The water transfer behavior across the membrane is a result of two major phenomena: the electro-osmotic drag from the anode to the cathode and back-diffusion from the cathode to the anode. Here, the water concentration (c_v) was assumed to change linearly. The following equation was used to capture this phenomenon:

$$\dot{m}_{v,membrane} = M_vA_{fc}n\left(n_d\frac{i}{F} - D_\omega\frac{(c_{v,av} - c_{v,an})}{t_m}\right) \quad (19)$$

where t_m is the thickness of the membrane, n_d is the electro-osmotic coefficient, D_ω is the diffusion coefficient, which varied with the water content in the membrane, M_v is the vapor molar mass, A_{fc} is the fuel cell active area, and n is the number of fuel cells in the stack [13].

The membrane water content (λ_m) was calculated using the following equation:

$$\lambda_m = \begin{cases} 0.043 + 17.81a_i - 39.85a_i^2 + 36.0a_i^3 & (0 < a_i \le 1) \\ 14 + 1.4(a_i - 1) & (0 < a_i \le 3) \end{cases} \quad (20)$$

where a_i is the water activity, which can be calculated using Eq. (21).

$$a_i = \frac{a_{an} + a_{ca}}{2} \quad (21)$$

The electro-osmotic and diffusion coefficients were calculated using Eqs. (22) and (23):

$$n_d = 0.0029\lambda_m^2 + 0.05\lambda_m - 3.4 \times 10^{-19} \quad (22)$$

$$D_\omega = D_\lambda \exp\left(2416\left(\frac{1}{303} - \frac{1}{T_{fc}}\right)\right) \quad (23)$$

where

$$D_\lambda = \begin{cases} 10^{-6} & (\lambda_m < 2) \\ 10^{-6}(1 + 2(\lambda_m - 2)) & 2 \le \lambda_m \le 3 \\ 10^{-6}(-1.67(\lambda_m - 3) & 3 < \lambda_m \le 4.5 \\ 1.25 \times 10^{-6} & 4.5 \le \lambda_m \end{cases} \quad (24)$$

T_{fc} is the temperature of the fuel cell.

2.2. Electrochemical model

The electrochemical model was primarily used to address the electric property of the PEM fuel cell stack.

The fuel cell voltage model was developed by subtracting the three major over potentials from the open circuit voltage:

$$V_{cell} = E_0 - V_{act} - V_{ohm} - V_{conc} \quad (25)$$

where E_0 is the cell open circuit voltage, also known as the thermodynamic potential, was calculated using Eq. (26).

$$E_0 = 1.229 - 0.85 \times 10^{-3}(T_{fc} - 298.15) + 4.3085 \times 10^{-5}T_{fc}\left[\ln(p_{H_2}) + \frac{1}{2}\ln(p_{O_2})\right] \quad (26)$$

The activation over potential was caused by the slow charge transfer reaction at the surface of the electrodes. Some of the electrode potential is used to drive the electron transfer to match the current demand; thus, the potential at the fuel cell terminal is reduced.

The activation over potential was determined using the following equation:

$$V_{act} = a\ln\left(\frac{i}{i_0}\right) \quad (27)$$

where i is the current density, i_0 is the exchange current density. i_0 and a are all constants and they were determined empirically.

The ohmic over potential occurs due to the resistance to the flow of ions in the electrolyte; the resistance to the flow of electrons through the electrodes and the contact resistance at the cell terminals. The ohmic over potential (V_{ohm}) can be determined using the following equation:

$$V_{ohm} = iR_{ohm} = i\frac{t_m}{\sigma_m} \tag{28}$$

where R_{ohm} is the internal electrical resistance, t_m is the thickness of the membrane, and the membrane conductivity is σ_m, which can be calculated using the membrane water content λ_m and the fuel cell temperature T_{fc}.

The value of the membrane water content (λ_m) varies between 0 and 14, which is equivalent to the relative humidity from 0% to 100%, respectively.

$$\sigma_m = (b_{11}\lambda_m - b_{12})\ \exp\left(b_2\left(\frac{1}{303} - \frac{1}{T_{fc}}\right)\right) \tag{29}$$

The constants b_{11}, b_{12} and b_2 are typically determined empirically [13].

The concentration over potential occurs due to a decrease in the concentration of the reactants at the electrode–electrolyte interface. A steady supply of the reactants is required at the electrode–electrolyte interface to maintain the flow of electric current. Due to diffusion or convection issues in the electrolyte, the concentration of the reactants is not maintained at the initial level. This over potential (V_{conc}) was calculated using the following equation:

$$V_{conc} = 1\left(c_2\frac{i}{i_{max}}\right)c_3 \tag{30}$$

where c_2, c_3, and i_{max} are constants that were determined empirically. The i_{max} is the limiting current.

Because the individual cells were stacked in series, the stack voltage was calculated using Eq. (31):

$$V_{st} = n \times V_{fc} \tag{31}$$

where n is the number of cells.

2.3. Air and hydrogen supply model

In this study, the air was assumed to be instantaneously supplied to the fuel cell stack cathode by an electronic blower, and the flow rate was calculated as a function of the required fuel cell current:

$$\dot{m}_{ca,in} = (1+\omega_{atm})\dot{m}_{dry\,air} = (1+\omega_{atm})\frac{1}{x_{O_2}}\lambda_{O_2}M_{O_2}\frac{nI_{st}}{4F} \tag{32}$$

where λ_{O_2} is the oxygen excess ratio and ω_{atm} is the air humidity ratio.

The hydrogen was supplied from a hydrogen tank and controlled using a solenoid valve. The flow rate was also calculated as a function of the required fuel cell current:

$$\dot{m}_{an,in} = \lambda_{H_2}M_{H_2}\frac{nI_{st}}{2F} \tag{33}$$

where λ_{H_2} is the hydrogen excess ratio.

3. Fuel cell–battery power system auxiliary model

3.1. Air blower model

The blower model introduced in this study is a general compressor/blower model previously discussed in [2] that uses the pressure difference between the blower inlet and outlet and the blower efficiency to calculate the power consumed by the blower.

The inlet and outlet temperatures and pressures are defined as T_1, T_2, p_1 and p_2, respectively.

$$\frac{T_2}{T_1} = \left(\frac{p_2}{p_1}\right)^{\gamma-1/\gamma} \tag{34}$$

where γ is the ratio of the specific heat capacities of the gas (c_p/c_v). The following assumptions were used to simplify the calculation.

1. The heat generated by the mechanism was neglected.
2. The change in kinetic energy between the inlet gas and the outlet gas were negligible.
3. The gas specific heat at constant pressure (c_p) was considered to be constant during the compression process.

Under the above assumptions, enthalpy is the only state that is changed by the mechanical work, resulting in the following equation:

$$\dot{W} = c_p(T_2 - T_1)\dot{m}_{gas} \tag{35}$$

$\dot{m}_{gas}$ is the mass rate of the compressed gas. The above formula represents the isentropic process because the exit temperature for the real work will be higher than the isentropic temperature:

$$\dot{W}^* = c_p(T_2^* - T_1)\dot{m}_{gas} \tag{36}$$

$\dot{W}^*$ and T_2^* are the real work of compression and the real exit temperature, respectively. The ratio between the isentropic work and the real wok can be calculated; this ratio is known as the isentropic efficiency.

$$\eta_{cp} = \frac{\text{isentropic work}}{\text{real work}} = \frac{c_p(T_2 - T_1)\dot{m}_{gas}}{c_p(T_2^* - T_1)\dot{m}_{gas}} = \frac{T_2 - T_1}{T_2^* - T_1} \tag{37}$$

By combining Eqs. (35) and (37), the equation shown below is found.

$$\eta_{cp} = \frac{T_1}{T_2^* - T_1}\left[\left(\frac{p_2}{p_1}\right)^{\gamma-1/\gamma} - 1\right] \tag{38}$$

The temperature difference is shown in Eq. (39):

$$\Delta T = T_2^* - T_1 = \frac{T_1}{\eta_{cp}}\left[\left(\frac{p_2}{p_1}\right)^{\gamma-1/\gamma} - 1\right] \tag{39}$$

The combination of Eqs. (35) and (39) results in the following equation.

$$\text{Power} = \dot{W}^* = c_p\frac{T_1}{\eta_{cp}}\left[\left(\frac{p_2}{p_1}\right)^{\gamma-1/\gamma} - 1\right]\dot{m}_{gas} \tag{40}$$

This calculated power is the mechanical power required to raise the gas pressure. To calculate the electric power consumed by the blower, the efficiency between the driving motor and the turbine must be considered. In this study, the efficiency was specified as 85%, according to the AMETEK 3.0 BLDC 12 VDC Low-voltage Blower data sheet.

3.2. DC/DC converter model

DC/DC converters are used to regulate the fuel cell output power by converting the rapidly changing fuel cell output voltage to a stabilized value to meet the requirements of electronics. In this study, the selected fuel cell stack output voltage was less than 10 V. For the power to be used for a standard electronic device, the voltage was boosted to 12 V, which is the nominal voltage for auto electronics and small portable electronic devices. Thus, the 12 V boost DC/DC converter was chosen for this study, and its efficiency was assumed to be 85% [25].

Fig. 1 shows the principle of a general switching boost DC/DC converter.

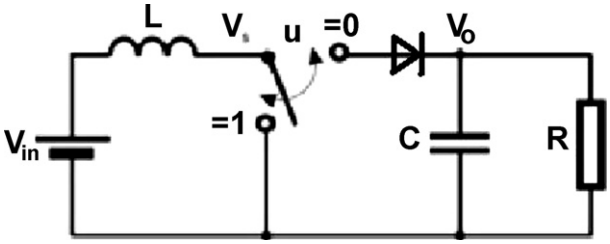

Fig. 1. Boost DC/DC converter.

The ON–OFF state demonstrated for a boost DC/DC converter is shown in Fig. 2.

The basic principle of a boost converter includes 2 distinct states (see Fig. 2).

In the ON-state, the switch (see Fig. 2) is closed, resulting in an increase in the inductor current.

In the OFF-state, the switch is open and the only path offered to the inductor current is through the fly back diode, the capacitor (C) and the load (R). This results in the transfer of the energy accumulated during the ON-state into the capacitor.

Based on the basic principle of this DC/DC converter, a mathematical model was derived as follows [26]:

$$C\frac{dv_c}{dt} = (1-u)i_L - \frac{v_0}{R} - i_0 \tag{41}$$

$$L\frac{dv_c}{dt} = v_0 - (1-u)v_0 - R_L i_L \tag{42}$$

$$v_0 = \frac{Rv_c}{R+R_c} + \frac{RR_c}{R+R_c}(i_L - i_0) \tag{43}$$

where R_L is a body resistor of the inductor and R_c is the equivalent series resistor of the capacitor.

3.3. Battery model

The generic battery model developed by Tremblay [27] is a simple battery model; however, it can be used to capture the primary behaviors of the battery. Thus, the lithium-ion battery model introduced by Tremblay [27] was employed in this paper.

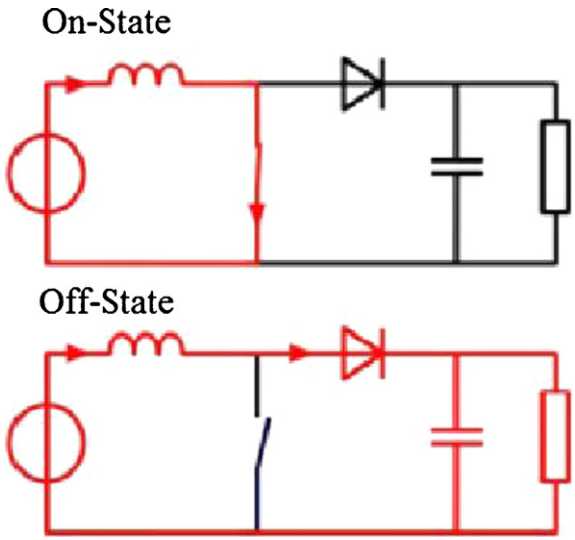

Fig. 2. ON–OFF state explained of boost DC/DC converter.

Discharge model ($i_d > 0$):

$$f_1(Q_{ext}, i_d, i_{batt}) = E_0 - R\cdot\frac{Q}{Q-Q_{ext}}\cdot i_d - R\cdot\frac{Q}{Q-Q_{ext}}\cdot Q_{ext} + V_{exp}(-Q_{exp}\cdot Q_{ext}) \tag{44}$$

Charge model ($i_d < 0$):

$$f_2(Q_{ext}, i_d, i_{batt}) = E_0 - R\cdot\frac{Q}{Q_{ext}+0.1\cdot Q}\cdot i_d - R\cdot\frac{Q}{Q-Q_{ext}}\cdot Q_{ext} + V_{exp}\cdot\exp(-Q_{exp}\cdot Q_{ext}) \tag{45}$$

State of charge (SOC):

$$SOC = 100\left(1 - \frac{\int_0^t i_{batt}dt}{Q}\right) \tag{46}$$

where E_0 = open circuit voltage (V), R = internal resistance (Ω), i_d = low frequency current dynamics (A), i_{batt} = battery current (A), Q_{ext} = extracted capacity (Ah), Q = maximum battery capacity (Ah), V_{exp} = exponential voltage (V), and Q_{exp} = exponential capacity ($(Ah)^{-1}$).

4. System controls and simulation results

4.1. Air supply control

Previous studies have proposed different types of control strategy for the air supply control in PEM fuel cells. Most of these methods used different types of feedback control, which collects different system states using many sensors and designs a high robustness controller to tolerate system uncertainties. In doing so, the controller could theoretically produce accurate results; however, it significantly increases the system cost and the heavy load calculation is not suitable for implementation into the embedded controllers. In contrast, it is known from experiments that the most serious current challenge for the unstable operation of PEM fuel cells is a liquid water problem, which cannot be solved by model-base control alone. This is because there is no non-CFD model that is able to address the liquid water behavior in a PEM fuel cell, and CFD models cannot be used for control development. Therefore, in our application, feed-forward control for the air supply system was the best choice. The feed forward control in our application presents several advantages.

i. It does not introduce instabilities.
ii. It does not rely on measurements of the system's state, which were much slower than the dynamics of the system in this particular case.
iii. It relies on a measurement of the system's only disturbance (I_{st}), which we can be obtained inexpensively with high precision and a large bandwidth.
iv. It reduced the computational load for the embedded controller.

The feed forward control algorithm for air supply control is shown in Fig. 3. The load required current was measured using a current sensor as the load following signal and then converted into a digital signal. The load following signal acts as the only input for the feed forward controller. The feed forward coefficient was calculated as a function of the load using Eq. (32). After the calculation, the feed forward controller provided the Pulse Width Modulation (PWM) command through the PWM module and directly controlled the air blower speed so that the flow rate at the cathode inlet could be controlled.

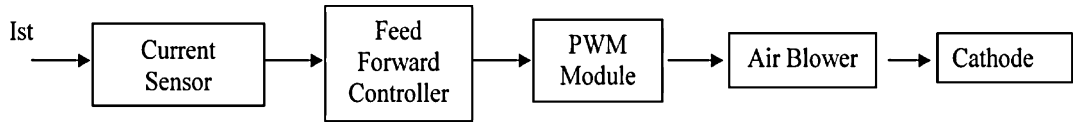

Fig. 3. Feed forward control algorithm for PEM fuel cell air supply control.

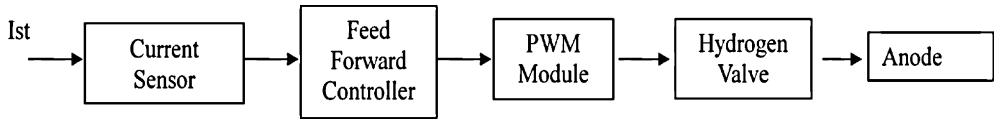

Fig. 4. Feed forward control algorithm for PEM fuel cell hydrogen supply control.

4.2. Hydrogen flow control

Using the same principle as the air supply control, the hydrogen flow control was achieved using a simple feed forward controller, as shown in Fig. 4.

The feed forward coefficient can be calculated as a function of the load following using Eq. (33).

Using the feed forward controller for cathode and anode flow control, only one sensor is required to complete both tasks.

4.3. Simulation of PEM fuel cell stack system

After the system input was applied (air and hydrogen flows), the simulation results of the PEM fuel cell stack system with integrated controller were available for analysis.

The parameters used in this simulation were based on a large PEM fuel cell stack (40 kW fuel cell stack) to more clearly interpret the results.

Fig. 5 shows the PEM fuel cell polarization characteristic curve from the simulation results. This curve captures the real PEM fuel cell polarization behavior. The voltage curve decreases as the fuel cell current density increases due to the three major voltage overpotentials. The power curve is the product of the fuel cell current and the voltage. Therefore, system power first increases as the current density increases; however, when the current density reaches a specific value, it begins to decrease. Eventually the system power reaches zero when the output voltage reaches zero.

A serial step input signal (Fig. 6) was employed as the system input to test the fuel cell stack system model. With this input, the fuel cell voltage response to the current demand and the fuel cell transient could be investigated.

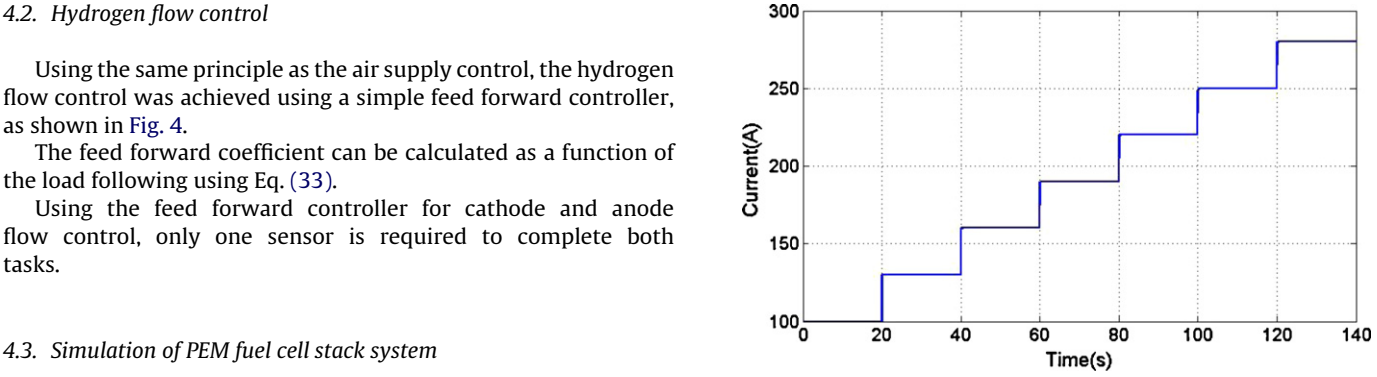

Fig. 6. Serial step load input.

The fuel cell output voltage response to the step input is shown in Fig. 7. As the current input increases, the output voltage decreases.

The PEM fuel cell voltage transient response is shown in Fig. 8. This figure shows the fuel cell voltage response during the external load change. It can be seen from this figure that when the input data changed from 100 A to 130 A, the voltage did not reduce to a steady level. Instead, it dropped to a lower value and recovered to a steady level after a period of time. This phenomenon was caused by the slow fuel cell transient response.

Fig. 9 shows the fuel cell output power response to the current step input increased. However, the increasing rate tended to be slower than before. This is because as the demanded current increases, the output voltage continues to decrease due to the fuel cell polarization behavior.

Fig. 10 shows the relative humidity change due to the step current input. Relative humidity is an important parameter, which directly affects the fuel cell output voltage. In the fuel cell anode,

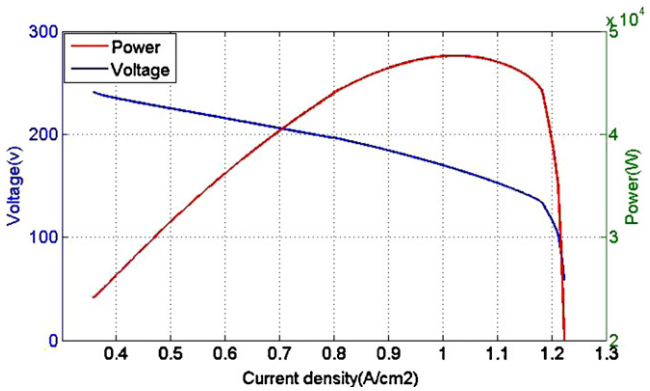

Fig. 5. PEM fuel cell polarization characteristic.

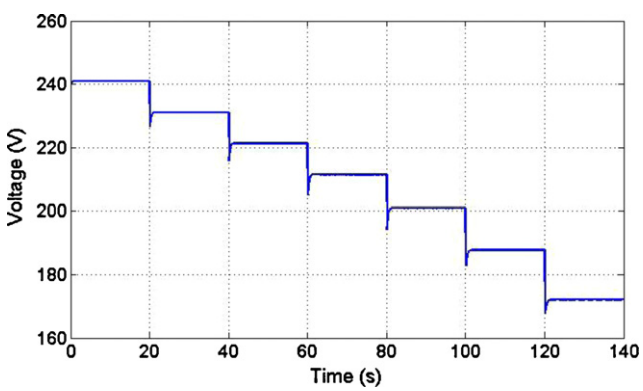

Fig. 7. Voltage response to step input.

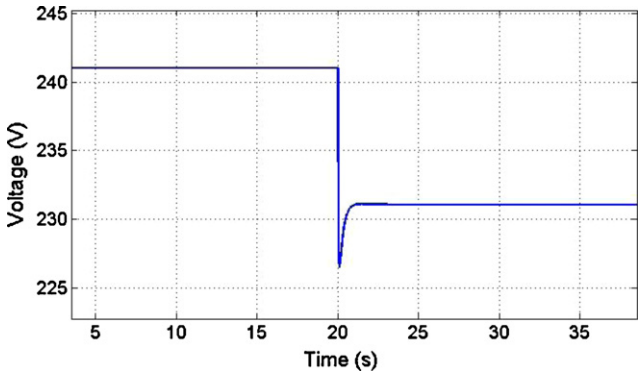

Fig. 8. Output voltage transient when input current change from 100 A to 130 A.

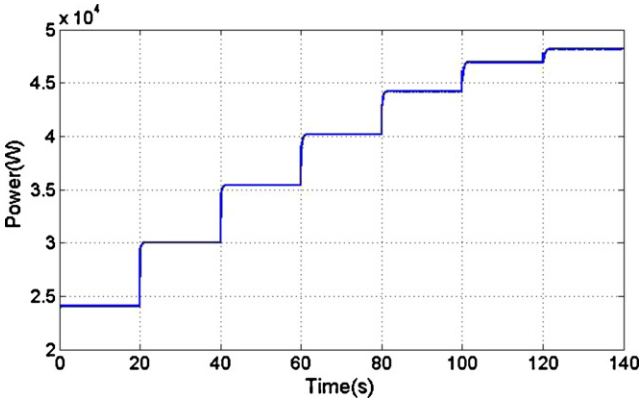

Fig. 9. PEM fuel cell output power response.

the RH decreases as the current density increases. This is because the electro-osmotic drag force becomes higher than the diffusion drag as the current density increases. The water tends to move from the anode to the cathode. Also, water is produced during the fuel cell operation; therefore, the RH in the cathode is always equal to one. This curve can be used for humidification control of the fuel cell operation.

4.4. Power management of PEM fuel cell–battery power system [28]

In this study, the power management algorithm is proposed based on the following rules.

When the load-required power is lower than the fuel cell–battery system rated power, which is 100 W in this study, the fuel cell will be employed to supply sufficient power to the load. The battery will only be used to supply power to the auxiliary systems. If the battery state of charge (SOC) is lower than its set lower bound, the fuel cell will start to charge the battery until the SOC reaches its set upper bound. During the charging time, the auxiliary systems will be powered directly by the fuel cell.

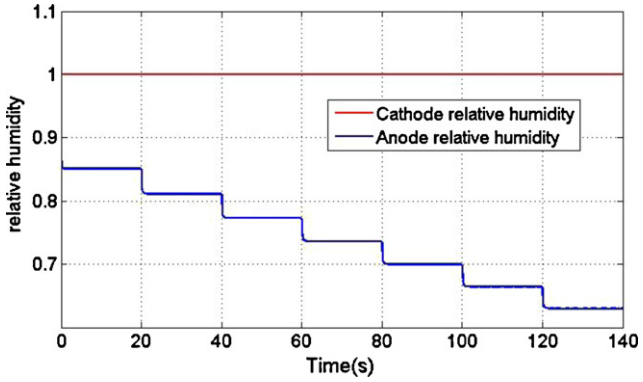

Fig. 10. Relative humidity change due to step current input.

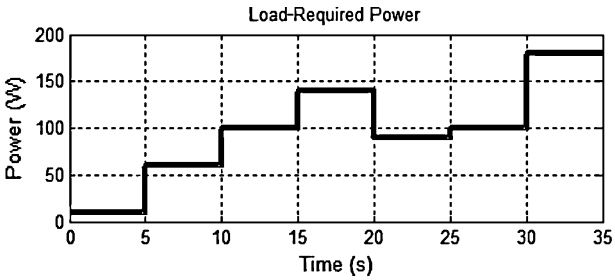

Fig. 11. Load-required power.

When the load-required power is higher than the system rated power but lower than 150% of the system rated power, the battery will be controlled to supply power simultaneously to the load and the fuel cell. The battery will not be charged whether the SOC is lower than the set lower bound or not. Auxiliary systems will be powered by the battery at all times.

When the load-required power is higher than 150% of the fuel cell–battery power system rated power, the system will automatically shut down the connection to the load to prevent damage to the load device and the fuel cell–battery power system.

4.4.1. Simulation conditions of power management system

All the mathematical models introduced above were implemented in the Simulink environment.

To capture the battery charging behavior in a short simulation time, a 12 V, 0.1 Ah lithium-ion battery was used. According to Kato in [29], the ideal SOC of a lithium-ion battery should be maintained at approximately 60% to extend its life. Therefore, in this study we chose the SOC upper bound to be 60%, the lower bound to be 58% and the initial SOC was specified at 60%.

The auxiliary-consumed power was the sum of the power consumed by the blower, the solenoid valves and the microcontroller. The power consumed by the microcontroller was assumed to be 5 W as long as the operation continued.

4.4.2. Power management system simulation results and discussion

In this simulation, a series of step signals were used to represent the load-required power, which is the input to the system, as shown in Fig. 11. These step signals can be used to represent most cases in practical applications. At time 0 s, the load began to require power from the power system at 10 W. At 5 s, the required power increased to 60 W. At 10 s, the required power reached the power system rated power of 100 W. The first overload power, 140 W, began at 15 s; however, this was within the system's affordable power range, which was 150% of the rated power. At 20 s, the required power became stable at the rated power of 100 W until 30 s. At 30 s, the second overload power of 180 W occurred, which exceeded the 150% system rated power limit.

The simulation results are shown in Figs. 11–18.

Fig. 12 shows the fuel cell required current calculated by the power management system and sent to the fuel cell stack subsystem as an input. The fuel cell stack sub-system took the required current as the input and generated the fuel cell voltage and power, as shown in Fig. 13. The fuel cell voltage was regulated by a DC/DC converter to a constant 12 V, and the fuel cell power was reduced by 15% due to the efficiency of the DC/DC converter. The regulated DC

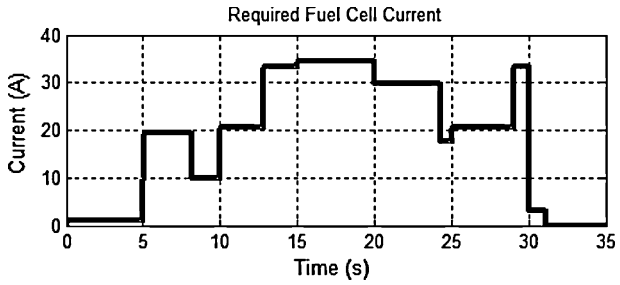

Fig. 12. Required fuel cell current.

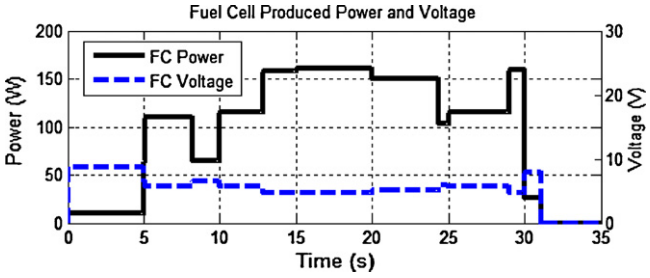

Fig. 13. Fuel cell produced power and voltage.

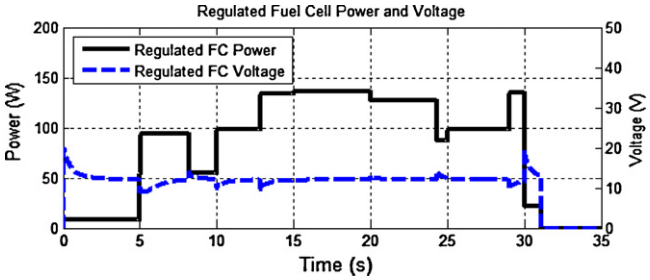

Fig. 14. Regulated fuel cell power and voltage.

power and voltage is shown in Fig. 14. The battery power is shown in Fig. 15. The positive power value represents the power supplied by the battery, and the negative values indicate that the battery was in the charging process. According to the battery power situation, the SOC is shown in Fig. 16. The auxiliary systems consumed power over time as shown in Fig. 17. The overall output power vs. the load-required power of the system is shown in Fig. 18.

The results show that in the first 5 s, the load-required power was only 10 W and only the fuel cell provided the power to the load. At 5 s, the load-required power increased to 60 W. The required fuel cell power increased; thus, the battery power consumed by the blower increased. At 5.2 s the battery SOC reached the lower bound of 58%, and the battery entered the charging phase. The fuel cell produced power increased simultaneously to charge the battery and supply the auxiliary systems. At 8 s, the battery SOC was charged to 60%; therefore, the fuel cell ceased charging the battery and the battery began to supply power to the auxiliary systems again. At 10 s, the load-required power increased to the system rated power of 100 W. The fuel cell could still sufficiently supply the load-required power and charge the battery during this process. At 15 s, the load-required power increased to 140 W, which is 40% higher than the system-rated power. During this situation, the fuel cell was not able to provide sufficient power for the load; therefore the power management controls required the battery to supply power to the load simultaneously with the fuel cell. At 18 s, the SOC was below the lower bound of 58%, and the battery was not charged because the power management controls prioritized supplying the load-required load. At 20 s, the load-required power was reduced to 90 W, which was lower than the system-rated power. The fuel cell began to charge the battery because its power was sufficient for charging. For the following 10 s, the load-required power was maintained at the system rated power to ensure that the system ran in a stable process. At 30 s, the load required is 180 W, which is more than 150% of the power system-rated power. Therefore, to protect both the load device and the system, the overload emergency shut down process was launched. The power system ceased providing power to the load. The fuel cell only provided power to the battery if it required charging, and the only power-consuming device in use was the microcontroller.

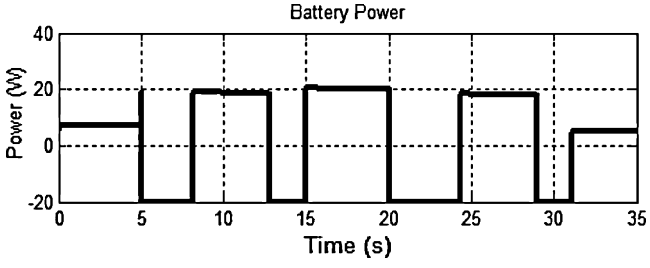

Fig. 15. Battery power.

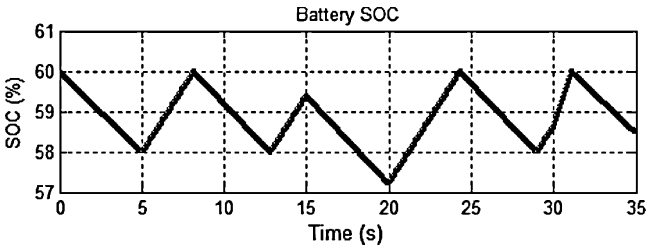

Fig. 16. Battery SOC.

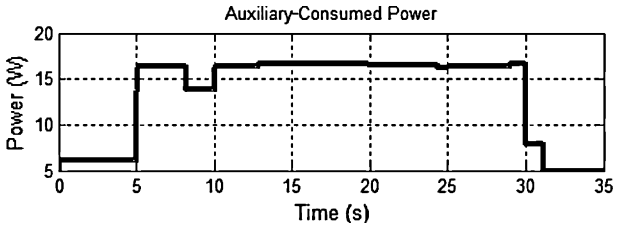

Fig. 17. Auxiliary-consumed power.

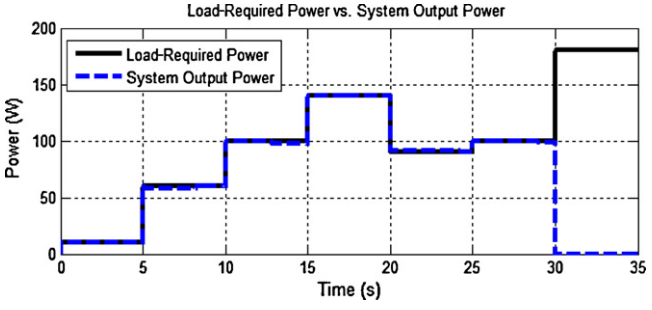

Fig. 18. Load-required power vs. system produced power.

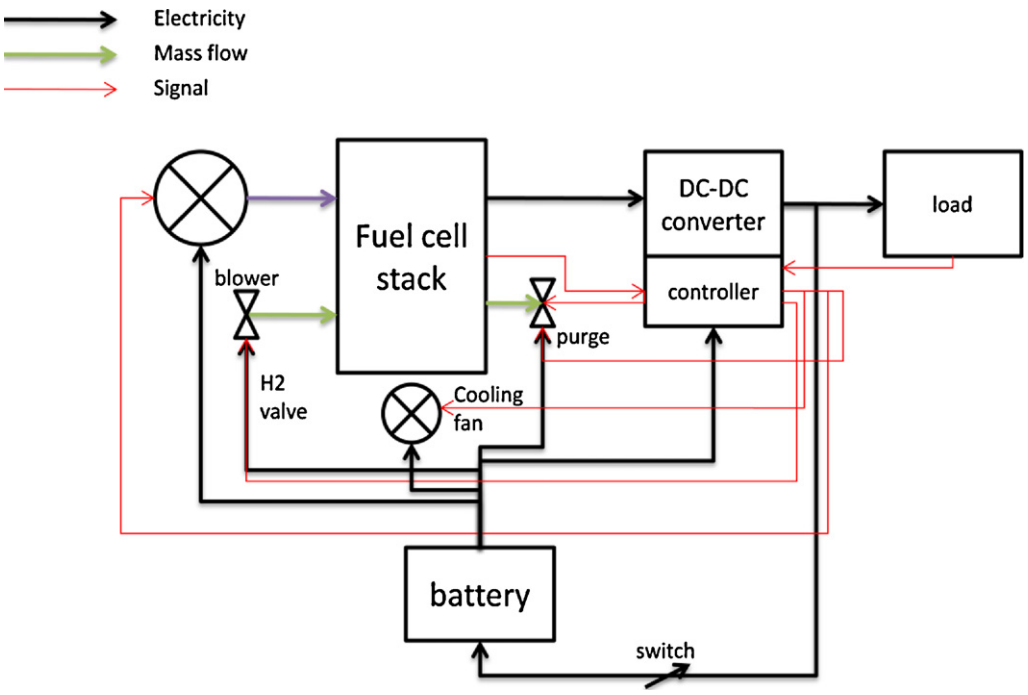

Fig. 19. Portable PEM fuel cell–battery power system diagram.

5. Portable PEM fuel cell–battery system with an embedded control system

5.1. System explanation

In this study, a 100 W portable PEM fuel cell–battery system was built to validate the designed controller performance and to investigate the PEM fuel cell performance.

A portable PEM fuel cell–battery power system diagram is shown in Fig. 19. In this system, a microcontroller was employed as the 'brain' of the system. The microcontroller used the demand current as an input and used a power management algorithm to calculate the power distribution. The PEM fuel cell stack was controlled by the blower and the hydrogen control valve. The battery charge or discharge was controlled using a switch. Temperature sensors were placed within the system, and a microcontroller monitored the system temperature through these sensors and sent a control signal to a cooling fan to control the system temperature.

5.2. Validation of the PEM fuel cell control system simulation

In this study, the 100 W PEM fuel cell–battery power system with an embedded control system was used to validate the simulation results. The fuel cell stack used here was a 100 W PEM fuel cell stack with 10 single cells and a cross-sectional area of 50 cm2.

The simulation environment was set up as the experimental environment with the following parameters:

i. room temperature,
ii. an initially well humidified stack was established by injecting liquid water, and
iii. the same inlet initial pressure and ambient outlet pressure.

The system inputs for the simulation and the experiment are shown in Fig. 20. A step current signal was employed. To obtain more accurate and clear results by minimizing the uncertainties, such as rapid temperature and relative humidity changes, we chose a low current density zone to test the fuel cell stack.

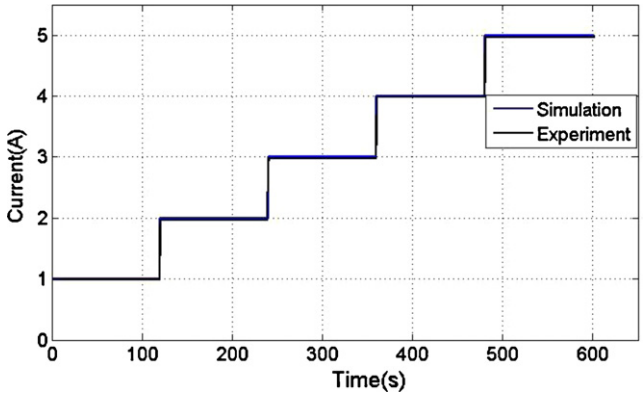

Fig. 20. Step current input for simulation and experiment.

Fig. 21 shows the voltage output of the system for the simulation and the experiment. The simulation results follow the

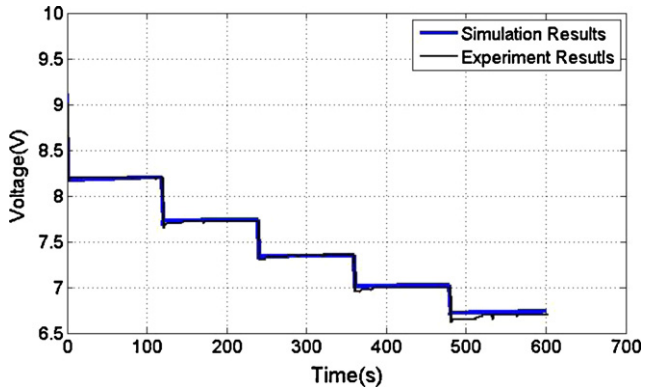

Fig. 21. Voltage output for simulation and experiment.

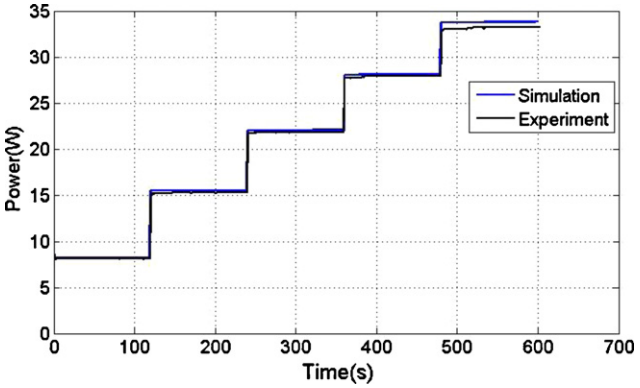

Fig. 22. Power output for simulation and experiment.

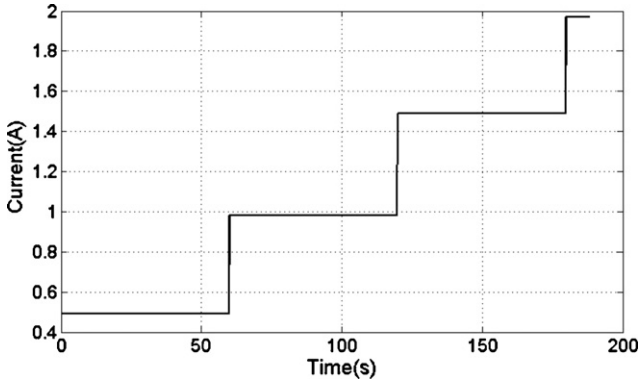

Fig. 23. Step current demand input.

trend of the experimental results. They correspond well for the first current (1 A) because in the initial state, all conditions in the simulation and the experiment were the same as defined at initialization. As the demand current increased, the experimental results became lower than the simulation results. The gap between the simulation results and the experimental result increased. This phenomenon was caused by two issues. (1) As the experiment continued, the relative humidity inside fuel cell stack decreased; thus, the output voltage decreased more than the simulation results. The decreasing relative humidity also caused the fuel cell operation response time to slow. (2) In the experiment, a 12 V DC 2 A blower was used as the air supply tool. The maximum output pressure of this blower was 0.5 psi, which meets the minimum requirement for this fuel cell stack. However, the fuel cell stack had a long, thin channel, which caused a significant pressure drop. Therefore, the actual cathode pressure was significantly lower than the blower output pressure. When the demand current was 1 A, the input flow rate of the fuel cell stack was sufficient; however, when the demand current increased, the fuel cell did not have sufficient oxygen as a reactant. Thus, the experimental output voltage decreased faster than the simulation results. This problem can be solved using a high-pressure blower; however, the larger blower will consume more power than the current blower. Because the blower power was provided by the fuel cell stack output power, it had a theoretical power limit of 100 W. Currently, a 12 V blower that can provide up to 5 psig of pressure and consume less than 100 W of power cannot be found.

Fig. 22 shows the power output for the simulation and the experiment. It follows the trend of the system voltage output. The increasing speed of the experimental results was becoming slower than the simulation results. The difference was also caused by air starvation and low relative humidity.

5.3. Portable PEM fuel cell–battery power system performance

The purpose of building a 100 W portable PEM fuel cell–battery power system was to use the PEM fuel cell stack as the main power source to provide continuous regulated DC power to electronics. Therefore, in the testing of the power system, we tested the regulated DC power output from the PEM fuel cell–battery power system. The expected result was a constant 12 VDC output voltage, which is not affected by the current demand like the fuel cell stack system. Therefore, this result did not require simulation results for validation.

A step current signal (shown in Fig. 23) was used in this experimental study as the system input.

Fig. 24 shows the system voltage output of the power system. For the first 180 s, the system output voltage was between 12 V and 11.8 V, which is acceptable for most electronics. However, beginning at 180 s, the system output became unstable. The instability was caused by the properties of the DC/DC converter. The DC/DC converter used in this work accepts an input voltage from 6 to 19 V DC, and the efficiency is approximately 80%, when the input voltage is between 9 and 15 V. When the current demand at the DC/DC converter output was 2 A, the actual current demand of the fuel cell stack was 5 A or more because the fuel cell stack output voltage at this time is approximately 7 V. At this point, the DC/DC converter efficiency becomes non-linear, which can lead to an efficiency less than 30%. The higher the current demand on the fuel cell stack, the lower the fuel cell stack voltage becomes. When the fuel cell stack output voltage was less than 6 V, the DC/DC converter ceased running. No commercial DC/DC converter that could accept an input voltage less than 6 V was found, as physically converting such a low voltage to a high voltage will cause a huge power loss. Therefore, the solution is either to build a DC/DC converter or use a fuel cell stack that can provide a higher output voltage.

Fig. 25 shows the fuel cell–battery power system output power. Due to the limitation of the low voltage output associated with the fuel cell stack, the system output cannot be higher than 18 W. However, as a demonstration project, these results show that the system can provide a continuous 12 V DC power supply to electronics as a power source.

From the results in Section 6, it is clear that there are some physical limitations of the hardware that prevent the PEM fuel cell–battery power system from achieving an improved performance. A high-pressure blower or air pump is required to prevent the fuel cell stack from air starvation when the demand current increases. To power the high-pressure blower or air pump and to increase the output voltage to fit the work-

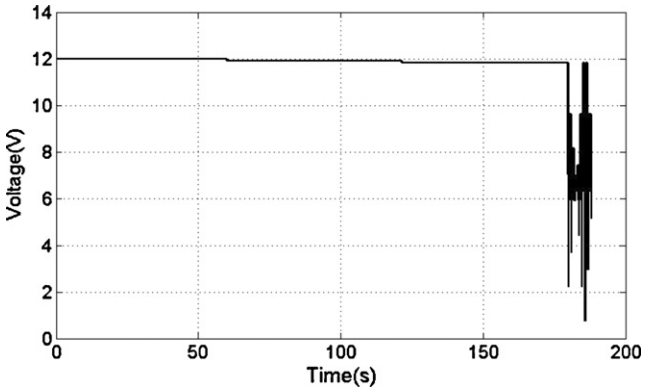

Fig. 24. System voltage output.

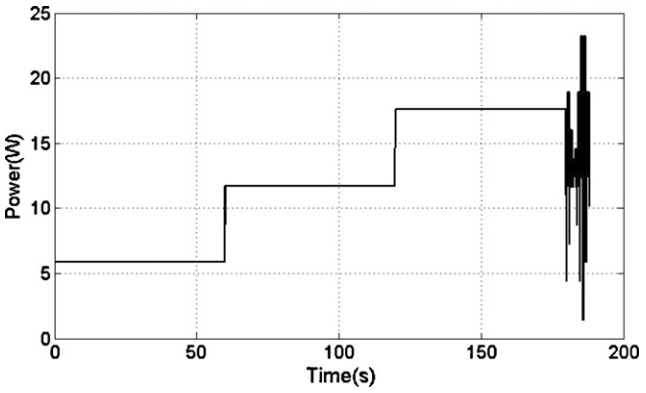

Fig. 25. System power output.

ing voltage range of the DC/DC converter, a larger fuel cell stack with a higher output voltage is recommended for further study.

Also, it is clear from the experimental results that the fuel cell output voltage response tends to be slower as the relative humidity decreases. A physical humidification system is required to improve the fuel cell system performance.

6. Conclusions

In this study, a general methodology of modeling, control and building a proton exchange membrane fuel cell–battery power system was developed. A set of PEM fuel cell–battery power system models was introduced. This model can be used to address the transience of the PEM fuel cell–battery power system and can be used as a platform for system controller development. A parametric study of the influences of the temperature, the relative humidity, the inlet pressure, and the oxygen excess ratio on the fuel cell performance was conducted based on this model. A set of PEM fuel cell–battery power system controllers was developed. The results show that the air supply control system could deliver sufficient reactants for the fuel cell stack; the humidification control system was able to increase the fuel cell system performance by maintaining the fuel cell stack relative humidity; and the system power management system was able to accurately distribute the demand power between the fuel cell and the battery and maintain the system components life and emergency shutdown. A physical PEM fuel cell–power system with embedded control system was built to validate the simulation results and to demonstrate the system. The validation results show that the simulation results correspond to the experiment results.

References

[1] R. O'Hayre, S.-W. Cha, W. Colella, F.B. Prinz, Fuel Cell Fundamentals, Wiley, 2006, ISBN 0-471-74148-5.
[2] J. Larmini, A. Dicks, Fuel Cell Systems Explained, John Wiley, Sons, Ltd, 2002.
[3] U.S. Department of Energy, Fuel Cell Handbook, 5th edition, 2000.
[4] J.H. Lee, T.R. Lalk, Journal of Power Sources 73 (1998) 229–241.
[5] S. Akella, N. Sivashankar, S. Gopalswamy, Proceedings of 2001 American Control Conference, 2001.
[6] J.C. Amphlett, R.M. Baumert, R.F. Mann, B.A. Peppley, P.R. Roberge, A. Rodrigues, Journal of Power Sources 49 (1994) 349–356.
[7] D.D. Boettner, G. Paganelli, Y.G. Guezennec, G. Rizzoni, M.J. Moran, Proceedings of 2001 ASME International Mechanical Engineering Congress and Exposition, 2001.
[8] J. Kim, S.-M. Lee, S. Srinivasan, Journal of the Electrochemical Society 142 (8) (1995) 2670–2674.
[9] M. Ogburn, D.J. Nelson, K. Wipke, T. Markel. Modeling and validation of a fuel cell hybrid vehicle. SAE Paper 2000-01-1566.
[10] R. Andrew, X.G. Li, Journal of Power Sources 102 (2001) 82–96.
[11] S.-H. Ge, B.-L. Yi, Journal of Power Sources 124 (2003) 1–11.
[12] X. Yu, B. Zhou, A. Sobiesiak, Journal of Power Sources 147 (2005) 184–195.
[13] J.T. Pukrushpan, A.G. Stefanopoulou, H. Peng, Control of Fuel Cell Power Systems, Principles, Modelling, Analysis and Feedback Design, Springer Verlag, 2004, ISBN: 1852338164.14.
[14] L. Benini, A. Bogliolo, G.D. Micheli, IEEE Transactions on Very Large Scale Integration (VLSI) Systems 8 (June (3)) (2000) 299–316.
[15] L. Benini, G.D. Micheli, Dynamic Power Management: Design Techniques and CAD Tools, Kluwer Academic Publishers, Norwell, MA, 1998.
[16] T.D. Burd, T.A. Pering, A.J. Stratakos, R.W. Brodersen, IEEE Journal of Solid-State Circuits 35 (November (11)) (2000) 1571–1580.
[17] L.H. Chandrasena, M.J. Liebelt, Proceedings of the International Symposium on Circuits and Systems, 2000, pp. 525–528.
[18] Y. Cho, N. Chang, C. Chakrabarti, S. Vrudhula, Proceedings of the 43rd Annual Conference on Design Automation, San Francisco, CA, USA, July 24–28, 2006.
[19] K. Choi, R. Soma, M. Pedram, Proceedings of the 41st Annual Conference on Design Automation, San Diego, CA, USA, June 07–11, 2004.
[20] E. Chung, L. Benini, G.D. Micheli, Proceedings of the 1999 IEEE/ACM International Conference on Computer-aided Design, San Jose, California, United States, November 07–11, 1999, pp. 274–279.
[21] L. Gao, Z. Jiang, R.A. Dougal, IEEE Transactions on Aerospace and Electronic Systems 41 (January (1)) (2005) 346–355.
[22] W. Gao, IEEE Transactions on Vehicular Technology 54 (May (3)) (2005) 846–855.
[23] D. Gervasio, S. Tasic, F. Zenhausern, Journal of Power Sources 149 (2005) 15–21.
[24] M.J. Gielniak, Z.J. Shen, Proceedings of the Vehicular Technology Conference (VTC) 6, 2004, pp. 4422–4426.
[25] AMETEK 3.0 BLDC 12 VDC Low-voltage Blower Data Sheet. Available from: www.ametek.com.
[26] Y. Cao, A Simulink Model Configurable to Buck, Boost and Buck–Boost DC–DC Converters with PWM PI Control, 2008. Available from: www.matlab.com.
[27] O. Tremblay, L.A. Dessaint, A.I. Dekkiche, Vehicle Power and Propulsion Conference, 2007. VPPC 2007. IEEE, September 9–12, 2007, pp. 284–289.
[28] Y. Zhang, B. Zhou, ASME 8th International Conference on Fuel Cell Science, Engineering and Technology, June 14–16, 2010, pp. 59–65.
[29] K. Kato, A. Negishi, K. Nozaki, I. Tsuda, K. Takano, Journal of Power Sources 117 (12) (2003) 118–123.